A priori simulation of relative permeabilities of intact subsamples of tight oil shale from a hydraulic fracturing play

G.Peter Matthews[1,2*], and *Katie* Jones[1]

[1]Department of Environmental Sciences, University of Plymouth, Devon, PL4 8AA, UK.
[2]PoreXpert Ltd, Exmouth, Devon, EX8 1BD, U.K.

Abstract. We present novel, *a priori* estimates of the nanoDarcy oil/water relative permeabilities within tight-oil shale that are too small to be measured experimentally, with the aim of increasing the yield from existing unconventional reservoirs. Intact half-cm^3 subsamples were washed to remove the mobile tight oil, then subjected to electron microscopy, mercury porosimetry, and helium and powder pycnometry. Simulated void networks were generated that are based on the PoreXpert inverse modelling of the entire mercury intrusion curve, extended to nanometer scale using helium pycnometry, with the completely integrated percolation behaviour of around 43000 voids of sizes closely matched to the experimental input. The absolute permeability of the network is calculated as the maximum flow through the pore-throat-pore arcs, determined by parametrised Navier Stokes equations. Relative permeability is modelled as a mobile phase moving past a static phase that restricts the flow. The resulting oil relative permeabilities vary according to the wettability of the sample surfaces. The unique characteristics of our results are that quasi-static and dynamic aqueous relative permeabilities vary according to local flow conditions, and that absolute relative permeabilities are presented that vary widely between samples, in contrast to the usual normalized values.

1 Introduction

Absolute gas permeabilities of tight-oil shale are very low, of the order of nanoDarcies, and therefore difficult to measure [1]. Although gas-liquid relative permeabilities in shale can be measured, oil/water relative permeabilities cannot. So the oil/water relative permeability characteristics inserted into reservoir models are often estimated from standard equations such as Brooks-Corey, an approach which is dubious even for conventional reservoirs [2]. We present a novel method of simulating oil/water relative permeability characteristics, based on precise inverse modelling of the full mercury intrusion characteristic extended down to micropore diameters with helium pycnometry.

The approach provides relative permeability estimates that vary with flow conditions, and that can be compared in absolute value between different samples. The preliminary results that we present are based on *a priori* physics with no calibration factors or semi-empirical fitting parameters. As described in Section 4, some validation of the core algorithms has been carried out, but further validation and calibration is required. The approach is therefore work in progress, rather than a calibrated and fully validated study.

Once completed, the new method has the potential significantly to improve the yield from existing tight-oil plays, not only by making existing reservoir models more precise, but also by giving an improved understanding of tight-oil retrieval in huff-puff scenarios, improved guidance for where to frack based on better characterisation of shale subsamples from cores, and by providing a better understanding of the reduction in yield with time, and hence better estimates of total field capacity.

2 Experimental

2.1 Sample selection

Cuboid subsamples were taken from a series of cores drilled from different depths of a tight-oil play. They had a side length of 0.76 ± 0.19 cm, and volume 0.41 ± 0.13 cm^3 (mean ± 1 standard deviation). Due to client confidentiality, the specific samples discussed here are generic rather than actual. Sample 1 is representative of the mid range of the samples we studied, and sample 2 is representative of low permeability outliers. To further protect client confidentiality, we give limited details of our detailed characterisations of the samples, and some results, such as extent of mercury porosimetry intrusion, are redacted. Nor can we provide measurements of absolute gas permeabilities, but based on our modelling, they are in the nanoDarcy to micro-Darcy range. The oil/water wettabilities of the samples are discussed below.

2.2 Sample cleaning

The standard process for cleaning core samples of infiltrated drilling fluids, salt and water, is the Gas Research Institute method for Soxhlet Extraction (1996), [3, 4], based on the Dean-Stark toluene solvent

* Corresponding author: matthewsgpeter@gmail.com

extraction [5]. This method involves refluxing liquid toluene to its vapour with boiling point 110 ^{O}C. A closed system is used in which the the vapour extracts oil and water from the sample. The water is condensed in a receiver vessel, and the toluene is continually cycled through the sample. When production of water ceases or the fixed period reflux has passed, the sample is then oven dried to remove any residual toluene.

Although toluene is the standard solvent to use for standard core samples, it is not suitable for tight samples. Toluene has a lower surface tension than water, so can wet the rock surfaces being exposed by the removal of the water, thereby lowering the overall chemical potential of the process. Furthermore, water has a small but significant solubility in toluene. So refluxing the sample for many days over an excess of toluene, while continuously stripping out the water, provides a slow but efficient and continuous method of water removal. This causes excessive desiccation of clays and shaley sandstones, by stripping the hydration water. Another concern over the use of toluene is the formation of secondary porosity from aggressive removal of bituminous material and kerogen from the shale [6].

Therefore in this project we have followed the suggestion of Cornwall [7], who advocated using iso-propyl alcohol (IPA) rather than toluene, to remove the infiltrated mud but leave any kerogen and bituminous material, thus reducing the likelihood of creating addition porosity during the cleaning process. However, that protocol specified refluxing for a week, which was impractical within the time constraint of this study. Therefore a preliminary study was carried out based on rotary evaporation of extracts of the IPA solvent at 24 hour intervals during the cleaning process, to leave a sludge residue. The sludge was dissolved in two drops of IPA, and pipetted onto an FT-IR plate. The IPA was then removed by blowing down with N_2. FT-IR spectral analysis of the solvent after 72 hours showed that the FT-IT spectrum was the same as the pure solvent, and that therefore sample extracts were no longer present. All interim spectra were discarded.

Following these analyses, the protocol was changed so that all samples were subjected to Soxhlet extraction for three days rather than seven. Methanol extraction for another three days was then used to displace and remove IPA and residual salts within the sample, since failure to perform a methanol extraction can lead to incorrect pore and grain volume measurements. Finally, samples were dried for a seven day period in a drying oven at 60 ^{O}C in accord with the API guidance for shale sample preparation or until the sample maintained a constant weight.

2.2 Characterisation

The cleaned subsamples were subjected to electron microscopy, helium pycnometry, powder pycnometry and mercury intrusion porosimetry, a combination of methods that we have previously used to characterise Gilsocarbon nuclear graphite [8].

Prior to electron microscopy, sample faces were polished using a series of ever finer wet and dry abrasive paper. Electron microscopy was used to survey the core samples to find regions for subsectioning which appeared likely to have contained mobile tight oil. Those regions were then examined in more detail, and natural cracks identified. Cracks were assumed to be natural, rather than generated by coring or subsampling, initially on the basis that one or both ends of the crack terminated within the samples. The surfaces of the natural cracks were examined using in-built electron dispersive spectroscopy (EDS) detectors as being carbon-rich, thus strongly implying that they had contained tight oil under oil-wet conditions. Successive 10 nm thick slices of exemplar samples including the natural cracks were prepared by focussed ion beam ablation (FIB-SEM), and SEM images of the slices were reconstructed to give 3D videos. These videos confirmed two further criteria for assuming that a crack was naturally formed, namely moderately or high tortuosity, and that opposite faces of the crack had differently shaped surface characteristics. The videos characterised volumes of sample of around 200 nm cubic side length. Such volumes were too small to provide a usefully representative sample volume, so the videos were only used for the identification of natural cracks, and not in the subsequent modelling. All subsamples for modelling contained natural cracks identified in this way. Typically two or three neighbouring subsamples were used for the various experiments. Although the neighbouring samples were selected to be within zones with the same mineralogy and crack characteristics, there nevertheless could have been some heterogeneity between the neighbouring subsamples. Due to the selection process, the subsamples were not representative of the overall shale cores, which contained large regions which appeared non-porous under electron microscopy, but only representative of those, often smaller, regions of the samples that contained natural cracks.

The modelling itself was based on properties covering the whole 0.4 cm^3 volumes of the cleaned samples, namely helium and powder pycnometry combined to give a precise accessible porosity of each sample, and mercury intrusion porosimetry up to an applied pressure of 400 MPa. The porosities determined in this way were: helium accessible void volumes as fractions of sample bulk volumes 0.21 ± 0.10, and from mercury intrusion 0.066 ± 0.039. These porosities are higher than they would be for typical subsamples of shale that had not been selected as containing natural cracks.

3 Modelling

3.1 Simulating the void network

The mercury porosimetry intrusion curves supplied most of the percolation characteristics of the samples. Traditionally, it is assumed that void features exposed to the mercury are cylindrical, with diameter d. Then the features intruded at an applied pressure P are calculated by the Laplace equation:

$$d = -\frac{4\gamma\cos\theta}{P} \quad . \qquad (1)$$

With respect to the mercury porosimetry in this work we use the commonly accepted value of 140° for the contact angle θ of mercury intruding sandstone against residual

air, and 0.48 Nm^{-1} for the surface tension γ, whereupon the numerator of Equation (1) becomes 1.47 Nm^{-1}. The uncertainties in these parameters have been discussed by Van Brakel [9]. Despite numerous published works to the contrary, it is not valid to assume that the void size distribution corresponds to the first derivative (slope) of the intrusion curve [10]. Such an approach implicitly assumes that the void structure comprises a bundle of capillary tubes, with sizes that differ but do not vary along their possibly tortuous lengths, aligned in the direction of fluid flow or percolation. To underline the avoidance of this false approximation, in this work the throat-entry sizes derived from Equation (1) are referred to as Laplace void diameters, Fig. 1.

As can be seen in Fig. 1, at the maximum applied mercury pressure of 400 MPa, the mercury intrudes pore-throat entry diameters of 4 nm, whereas in shale, tight oil can be confined in features smaller than that. If decane is taken as a proxy for tight oil, then its effective molecular diameter is around 0.7 nm. So molecules could occupy features of 1 nm and above. Molecules so constrained would be difficult or impossible to extract / produce, but the potential applications of the proposed method also include total reservoir capacity and the tail-off of production, so all possible tight-oil molecules need to be included.

For samples with homogeneous surfaces, pore sizes below 4 nm can be determined by interpreting N_2 and/or Kr adsorption isotherms using Density Functional Theory (DFT) or Grand Canonical Monte Carlo (GCMC) methods. The pore size distribution can then be converted to the equivalent percolation characteristic, by assuming that all voids are surface-accessible throats, so as to extend the experimental percolation characteristic, Fig. 1, to smaller sizes. However in the present study, the shale surfaces are heterogeneous and not characterizable by DFT or GCMC simulations. As neither simulation nor experiment is available to provide the percolation characteristic between the percolation at minimum size / maximum pressure and the helium pycnometry point, the simplest assumption has been made, namely a linear interpolation to give the intercept shown at 1 nm .

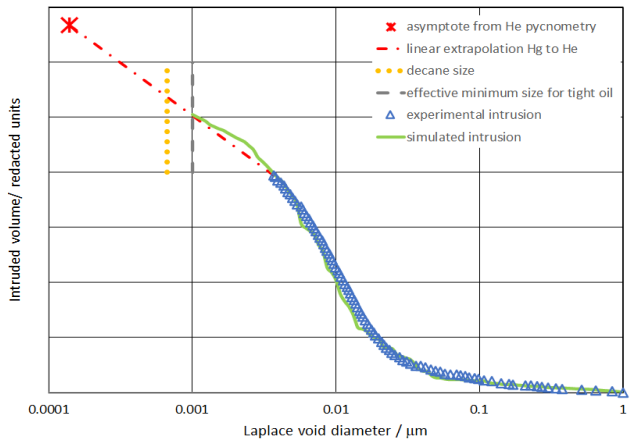

Fig. 1. Combined porosimetry and pycnometry for shale

At the low pressure / high diameter end of the intrusion characteristic, sample edge effects would produce an identifiable step, but no such step exists in Fig. 1. Intrusion at pressures lower than that corresponding to 1 µm via Equation (1) was negligible, as can be inferred from Fig. 1, so the modelled percolation curve was truncated to zero intrusion at that Laplace void diameter. The percolation characteristic used as input to the inverse modeller PoreXpert was therefore that shown in Fig. 1 between 1 nm and 1 µm.

Guided by a Boltzmann-annealed simplex, the inverse modeller generates a series of void structures with characteristics progressively closer to the experimental data. This is not simply a curve fitting exercise – the simplex searches 5-dimensional parameter space for void structures that fit the experimental data using experimentally related parameters: the void network connectivity, the degree of short-range structuring as described below, and the shapes and spread of the pore and throat-entry size distributions. The extent or shape of each parameter is characterised by a single number, normalised within parameter space to be of equal importance. The goodness of fit is measured by scaling the range of the x and y axes to 100%, and measuring the average distance δ of each experimental point to the closest simulation point within that two-dimensional parameter space. Consequently there is no constraint on the fit between 1 nm and 4 nm, because there is no experimental data within that range. For the fit shown in Fig. 1, $\delta = 1.4\%$.

The simulated void structure is in the form of a unit cell, Fig. 2, with periodic boundary conditions. It is an inverse image, in that voids are shown solid, and the solid phase is shown transparent, to facilitate viewing of the whole void network rather than just its outer surface. The network comprises cylindrical 'throats' connecting cubic nodes ('pores') in the three Cartesian directions. These shapes are simplistic, but when formed into a large network, provide a representation of the actual void volumes and topology to a useful degree of accuracy, within the context of the approximations and trade-offs required in generating a network model [11]. The size of the unit cell is adjustable. It was found that the minimum size of unit cell that would provide a fit to the percolation data over the three orders of magnitude in size was one based on a cubic grid of $\mathcal{N}$ pores in each Cartesian direction, where $\mathcal{N} = 25$. Although the number of pores is fixed in this way, the number of throats that join them is determined by the connectivity of the network. The unit cell shown in Fig. 2 comprises 15 625 pores and 27 460 throats, i.e. 43 085 fully integrated void features in total. As each throat connects two pores, the average coordination number in this case is 3.5. All percolation and permeability occurs from only the top face of the unit cell shown in Fig. 2 in the downward ($-z$) direction, as percolation from all sides produces an unrealistically early and sudden point of inflexion in the simulated percolation characteristic.

An important parameter not investigated by the simplex is the short-range size autocorrelation between pore-throats, or 'structure type'. The 'vertically banded'

structure type invokes bands of throats of similar size parallel to the -z direction of fluid flow for percolation and permeability. So in the vertically banded case the percolation is parallel to the layers. The appropriate degree of any structure type is characterised by a parameter σ that varies from 0 (random) to 1 (fully structured). For the unit cell shown in Fig. 2, σ = 0.18, so the degree of banding, emphasised by the intrusion of non-wetting fluid such as mercury from the top (maximum z) face, is not very marked. The 'horizontal large to small' structure type invokes layers of similarly sized pore-throats normal to the flow direction, Fig. 3. The effects of different structure types on the simulated percolation characteristic are accentuated by the periodic boundary conditions, and because the simulated percolation only occurs at the top face of every, semi-infinitely repeating, unit cell. In a natural sample, the actual short-range size autocorrelation would be between these two extremes, so the two structure types were used to give upper and lower bounds to the relative permeability simulations. A very few samples were even more extreme than the outliers represented by sample 2, in that they were almost impermeable to mercury up to 400 MPa applied pressure (average porosity 0.005), but nevertheless had significant porosity when immersed in helium. For these, the only structure type that fitted the results is exemplified in Fig. 4, i.e. large voids or clusters entirely surrounded by micropores of less than 4 nm diameter, such that the samples would be effectively impermeable to both water and oil, despite having a porosity measurable by helium. They were not included in the overall relative permeability simulations described below.

Inverse modelling gives a large range of possible void networks, all of which have percolation characteristics which closely match those of the experimental samples. Therefore at least five stochastic realisations for each structure type of each sample were generated. The various network fitting parameters are coupled due to their concerted convergence onto the experimental percolation characteristic. The representative structure was therefore taken to be that which had all parameters as close as possible to the means of the distribution of the values of the five or more stochastic generations. The convergence onto experimental percolation characteristics gives confidence that the behaviour of pore fluids within the representative simulated network is usefully similar to that in the experimental shale samples.

The inverse modeller identifies possible void clusters [10], as shown stippled in Figs. 2 and 3 overleaf, and numerically in Fig. 5. In the current relative permeability simulation, a cluster is assumed to behave in the same way as the envelope volume that it occupies.

The maximum asymptote of the cumulative Total Voids distribution in Fig. 5 is the sample porosity. The linear axes give little information about the sizes of the smallest voids that contain the tight oil. So a more informative plot is obtained using logarithmic axes, Fig. 6, which in this case shows the volumes as discrete rather then cumulative. Both figures emphasise that there is no maximum in the void size distribution around 10 nm, as would be inferred from the intrusion curve, Fig. 1, using the traditional first derivative (capillary bundle) assumption.

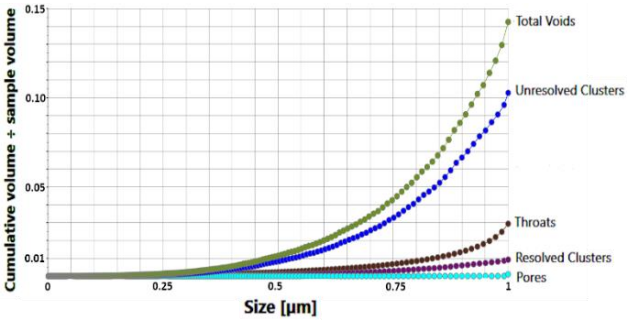

Fig. 5. Void size distributions for representative Sample 1

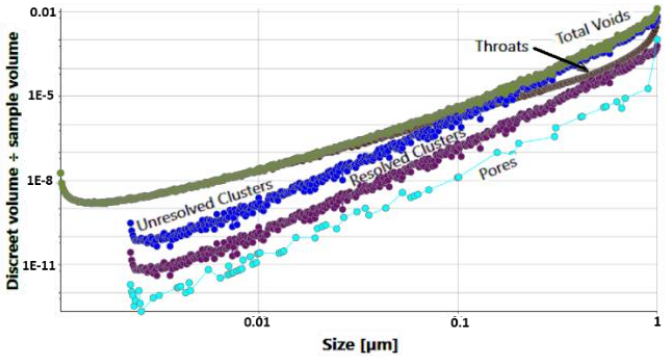

Fig. 6. The distributions shown in Fig. 3, but plotted on logarithmic axes with discreet rather than cumulative volumes.

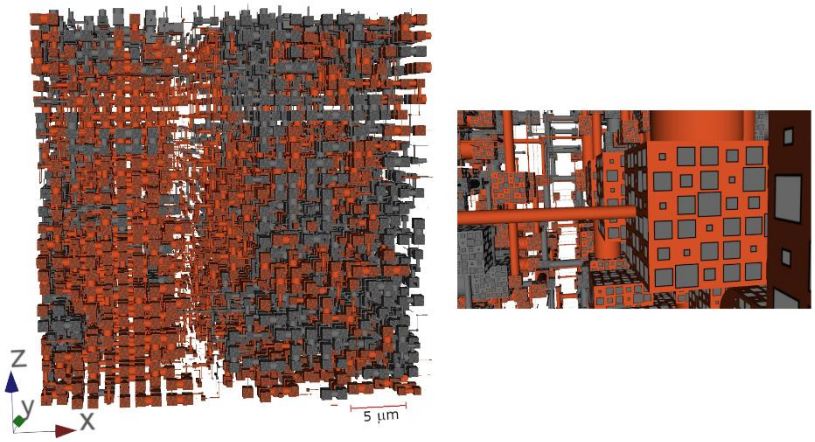

Fig. 2. The unit cell of the simulated void structure of shale, 40% percolated by a dark grey non-wetting fluid. Vertically banded structure type, giving upper permeability bound. Detail on the right of part of the nanoporous zone shows that even under magnification some of the nanoporosity is almost invisibly small.

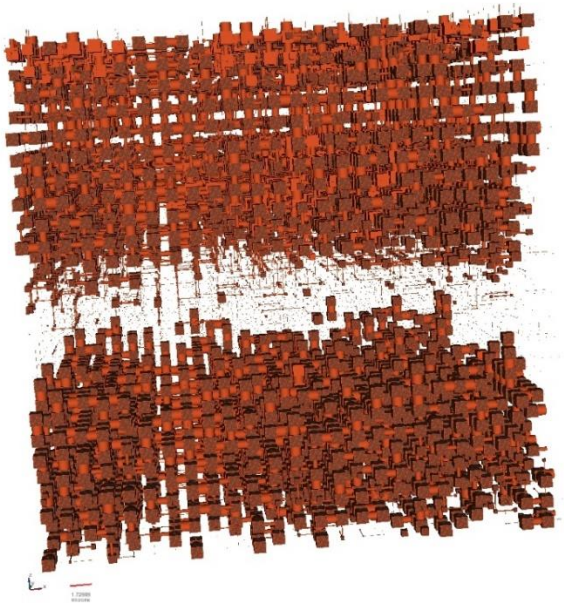

Fig. 3. Unit cell for sample 1 with horizontal banding, giving the lower permeability bound. Small scale bar 1.73 µm.

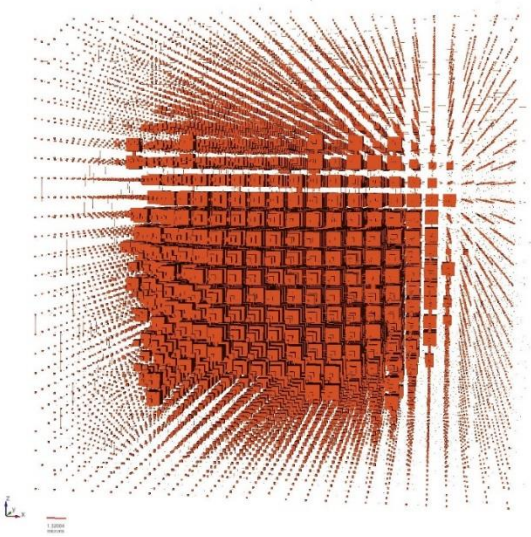

Fig. 4. The only structure type that would fit extreme outliers almost impermeable to mercury but with significant porosity accessible to helium, i.e. larger voids or void clusters entirely surrounded by micropores. Small scale bar 1.32 µm.

3.2 Permeability calculation

The permeability algorithm within the inverse modeller calculates the network permeability for liquids or gases. The permeability is independent of the solid phase, and only varies according to the geometry of the void network and the mean free path λ between collisions in the fluid.

For the calculation of permeability, each pore-throat-pore arc of the network has a flow capacity F_{arc} calculated from parametrized Navier-Stokes equations [12]:

$$F_{arc} = -\frac{8}{\pi}\left[\frac{1}{\frac{57}{4L_1^3\left(1+\frac{8.8\lambda}{L_1}\right)}+\frac{8h}{\pi r^4\left(1+\frac{4.4\lambda}{r}\right)}+\frac{57}{4L_2^3\left(1+\frac{8.8\lambda}{L_2}\right)}}\right] \quad (2)$$

where h is the length of a throat of radius r connecting two cubic pores with sides L_1 and L_2, respectively. The simultaneous solution of around 27500 arcs within the unit cell shown in Figs 2 and 3 is computationally intractable. So instead, an operational network algorithm (Dinic) is used to calculate the maximum capacity of the network. The result is an approximation of the total flow, in that it allows for separate flows of fluid through the same throat up to the maximum capacity of that throat, an approximation that we call 'trickle flow'. For the incompressible fluid case, this provides a useful approximation to the total flow capacity of a unit cell, but is likely to underestimate the total flow capacity for a gas. To emphasise the approximation, we refer to the results as void network capacities, not absolute permeabilities. Larger unit cells provide more realistic values of network void network capacity because there are fewer unit cell replications to represent the experimental sample, but computation time rises approximately as $\mathcal{N}^4$. For $\mathcal{N}$ = 25, computation time for a single permeability calculation with this trickle flow approximation on a fast, multi-threaded personal computer is of the order of 5 hours.

For gases, Eqn (2) scales precisely from laminar flow to Knudsen (slip) flow according to the relative length of λ and L. The effect of Knudsen flow is referred to as the Klinkenberg effect. It typically increases flow rates for gaseous N_2 near ambient pressure by around 1% for 1 μm throats. However, for the systems studied in this work, the relative increase in flow is around three orders of magnitude. The approach here differs from other studies in that the Knudsen flow correction is applied to each throat within the void network, rather than as a Klinkenberg factor for the whole sample typically correlated with permeability [1].

In the current study, both oil and water are liquids. For liquid systems, λ is ill-defined and we assume it to be zero. Although that should be a good approximation physically, experimental measurements of decane and hexadecane through photoresist (hydrocarbon polymer) channels of height h between horizontal confining plates of 50 nm to 130 nm [13] show a slip length Λ of 15 to 30 nm, where the flow rate Q_{slip} is increased from the flow rate Q_0 without slip according to :

$$Q_{slip} = Q_0\left(1+\frac{6\Lambda}{h}\right) \quad (3)$$

At an even smaller scale, flow can only be simulated rather than measured. The flow rate of gaseous argon in a single nanometre tube has been modelled by applying Navier-Stokes equations to a lattice-gas model [14], and shows deviations from laminar Poiseuillian flow, from which it can be inferred that liquids would also demonstrate deviations. Overall, however, our approximation that λ = 0 makes the computation over the whole network of around 16 000 pores and 27 000 throats both scalable and tractable. On the basis of slip flow alone, the results in [12] suggest that the permeabilities of the upper bounds described below, which are not so limited by flow through micropores, will be good approximations, whereas the lower bound permeabilities are likely to be too low.

3.3 Water relative permeability simulation

For an oil-wet sample, we calculate the aqueous relative permeability in the presence of static oil. The assumptions vary according to whether the situation is dynamic or static. By dynamic, we refer to the forced movement of water through the samples, such as during a water flood. We assume that oil coats the pores, but not the throats, to an equal film thickness through the sample. Fig. 7 shows diagrammatically that assumption applied to the macroporous, mesoporous and nanoporous regions of the sample. For static conditions, the oil films are assumed also to occupy throats, as shown, so obstruct channels within meso- and nano-porous regions as shown. The static assumption is shown applied to a small section of a shale unit cell in Fig. 8.

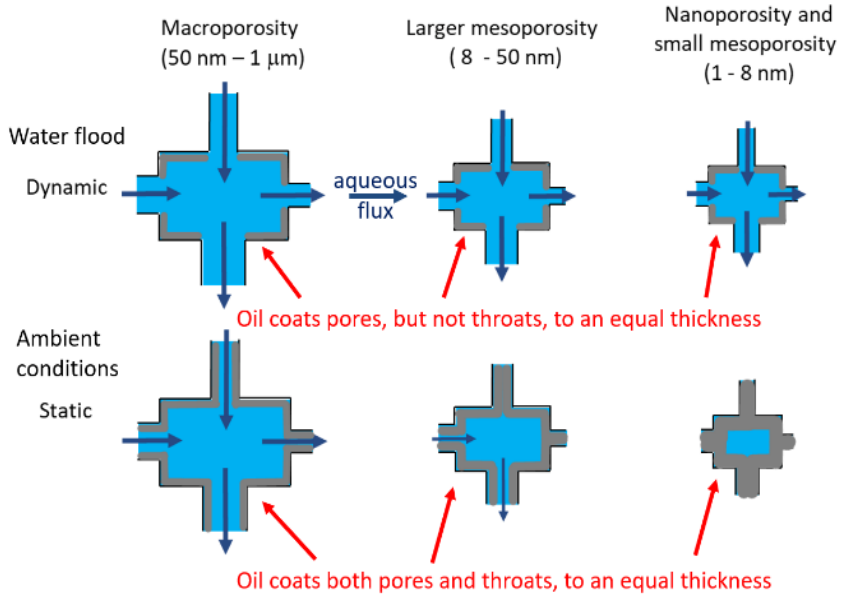

Fig. 7. Assumptions for the calculation of dynamic and static relperms

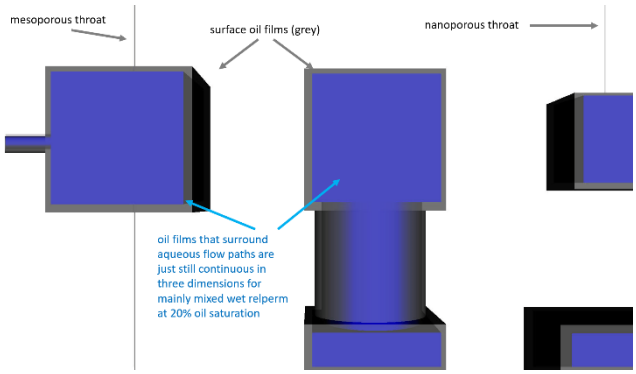

Fig. 8. Oil film within void features of a shale unit cell

Fig. 9 demonstrates that for the static case, the oil film blocks the micropores and small mesopores at very low oil saturation S_o of 0.006. The effect of this on the relative permeability is explained below.

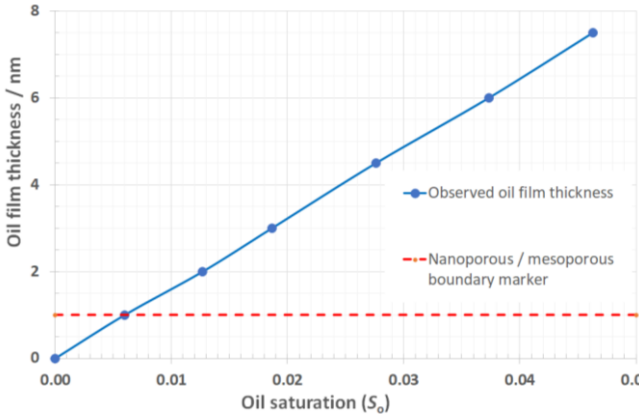

Fig. 9. Graph of thickness of the oil film illustrated in Fig. 8 versus oil saturation for the shale unit cell

Fig. 10 is a two-dimensional map of only the aqueous ganglia in the surface layer of the shale unit cell at an oil saturation S_o of 0.2.

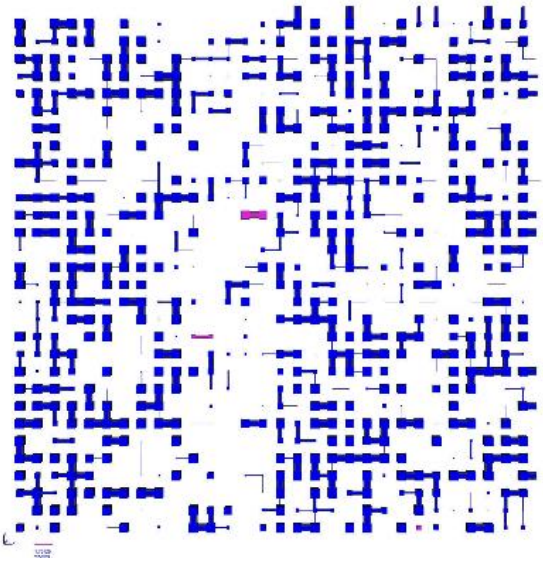

Fig. 10. 2D map of aqueous ganglia in the surface layer of the shale unit cell at S_0 = 0.2.

The resulting relative permeabilities are shown in Fig. 11. The graph shows the upper and lower bounds for the dynamic and static cases. As stated previously, for the upper bound, the unit cell structure type is parallel to the direction of flow, as in Fig. 2. For the lower bound, the structure type has banding perpendicular to the flow direction, Fig. 3. The most extreme effect of the oil film shown in Figs. 8 and 9 is for the lower bound of the static case. Here, oil blocks the throats in the band of micro- and meso-pores perpendicular to the direction of fluid flow, Fig. 3, so the permeability drops off very rapidly as water saturation decreases, as shown by the triangular symbols in Fig. 11.

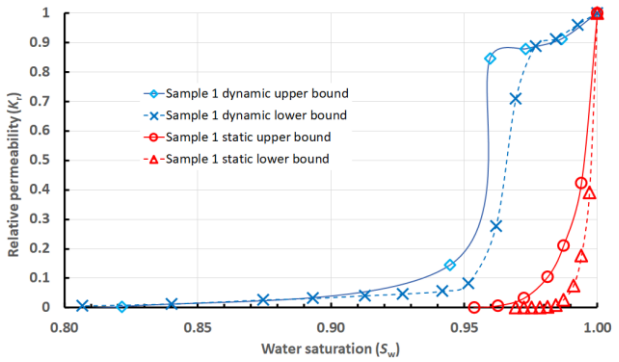

Fig. 11. Water relative permeabilities for an oil wet shale sample Table 1), shown with a linear relative permeability scale.

Every relative permeability calculation arises from a complete mapping of the flow within the unit cell, as shown in Fig. 12 overleaf for the upper, parallel bound.

3.4 Oil relative permeability simulation

For the calculation of oil relative permeabilities, disconnected aqueous ganglia are assumed to occupy and obstruct the central zones of all voids above a certain size, with the size dependant on the wettability of the shale surface layers. We do not have measured wettabilities our samples, although we assume from the EDS measurements mentioned earlier that they were very probably highly oil wet. Instead we have calculated relative permeabilities for a wide range of wettabilities, and report two examples in this work. The wettabilities are incorporated into the simulation via arbitrary qualitative descriptors linking them to aqueous ganglia size, as shown in Table 1.

Table 1. Aqueous ganglia sizes relative to qualitative oil wettability descriptors

Cylindrical aqueous ganglia can exist in voids above a diameter of	Qualitative description
500 nm	very highly oil wet
300 nm	highly oil wet
100 nm	medium high oil wet
30 nm	medium oil wet
10 nm	weakly oil wet
3 nm	mainly mixed wet
1 nm	entirely mixed wet

Fig. 13 shows aqueous ganglia within a small section of the shale unit cell with moderate water content in a medium high oil wet sample. As can be seen, the flow of oil around the static aqueous ganglia is annular. Again, to keep the computation of annular flow within the c. 27500 throats tractable, the annular flow is approximated as the equivalent flow through cylinders, as shown in Fig. 14. The approximation of static aqueous ganglia only obstructing features large enough to accommodate them does not allow for oil contents below those at maximum stable water content. So for very low oil concentration, proportional reduction of all features must be invoked, as shown on the right of Fig. 14 overleaf. This is equivalent to assuming that for very low oil concentrations, the oil was not present in the first place, rather than simply being displaced by water. The asymptote as $S_o \rightarrow 0$ is then as shown in Fig. 15.

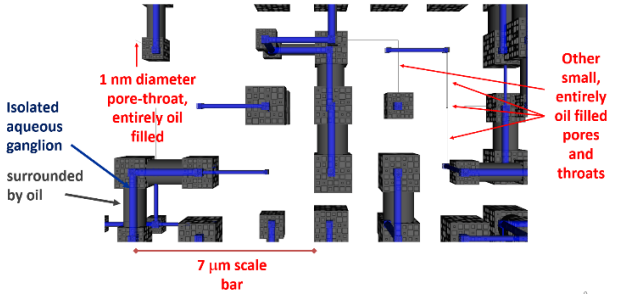

Fig. 13. Mapping of aqueous ganglia for a medium high oil wet sample

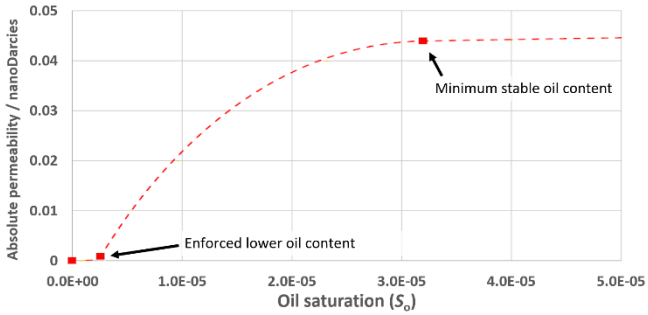

Fig. 15. Absolute oil permeability at very low oil saturation

Fig. 16 shows the oil relative permeabilities over the full range of water saturations. As for the water relative permeabilities, the oil relative permeabilities are based on full mappings of the oil permeability routes through the unit cell at each water saturation, as shown in Fig. 17 overleaf.

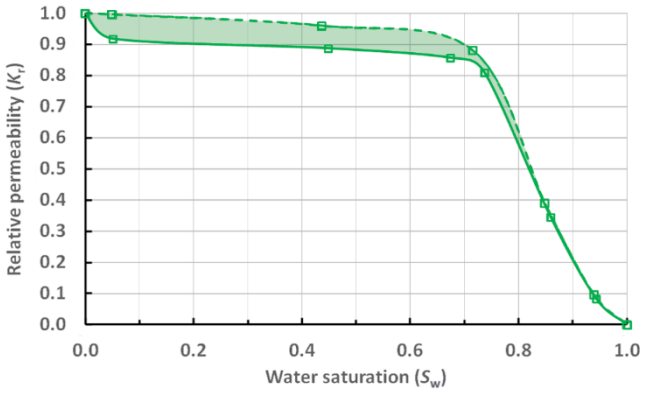

Fig. 16. The range of oil relative permeabilities between the upper and lower bounds over the full range of water saturation

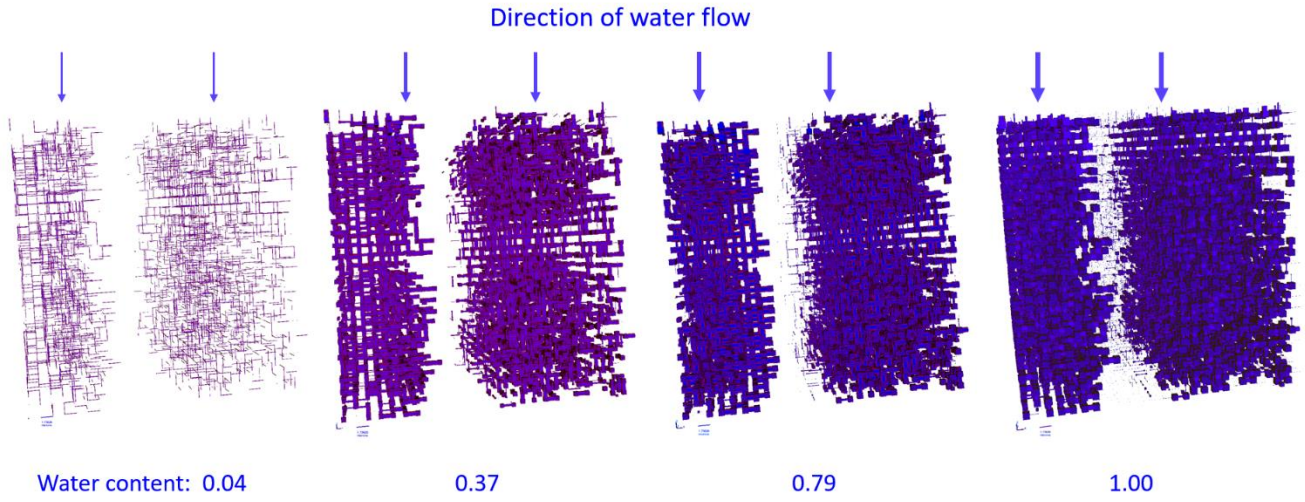

Fig. 12. Unit cells showing water flow mapping for the upper bound of the water relative permeabilities

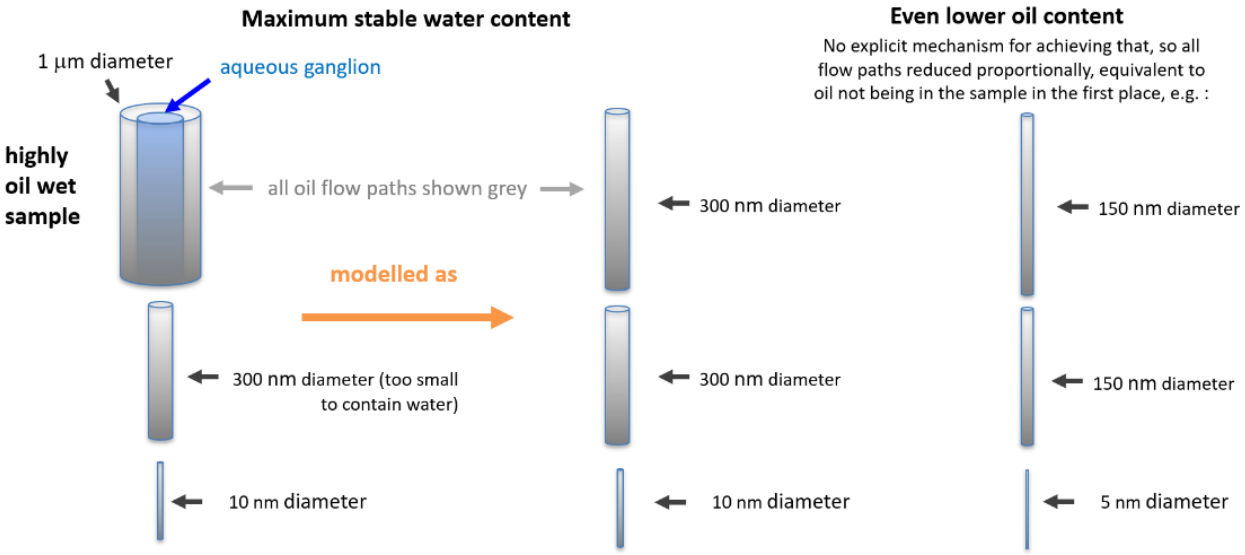

Fig. 14 . Approximations used for modelling the effect of static aqueous ganglia, and for even lower oil content

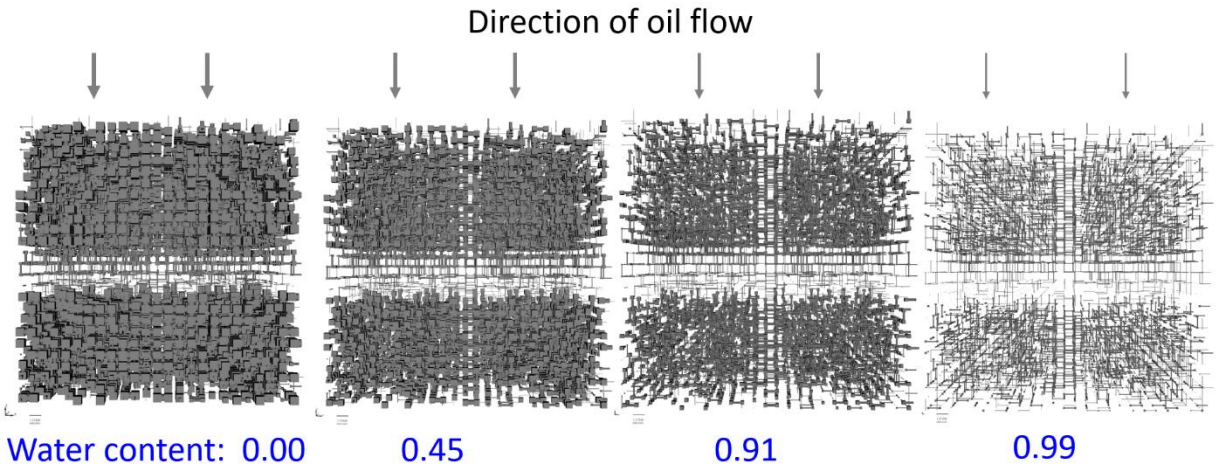

Fig. 17. Unit cells showing the oil flow mapping at increasing water saturations for the lower bound of the relative permeability calculations.

3.5 Absolute permeability simulation

Traditional relative permeability estimates are relative, all normalised to the same scale of e.g. 0 to 1, so much information about the difference between samples is lost. The PoreXpert inverse modeller has the important ability to estimate absolute void network capacities, although there is likely to be a discrepancy between those and absolute permeabilities as explained in Section 3.2 above. However, an indirect validation of the model, described below, supports the postulate that the relative differences in absolute permeabilities between samples trend correctly. Fig. 18 shows the results for Sample 1 and the low permeability outlier Sample 2.

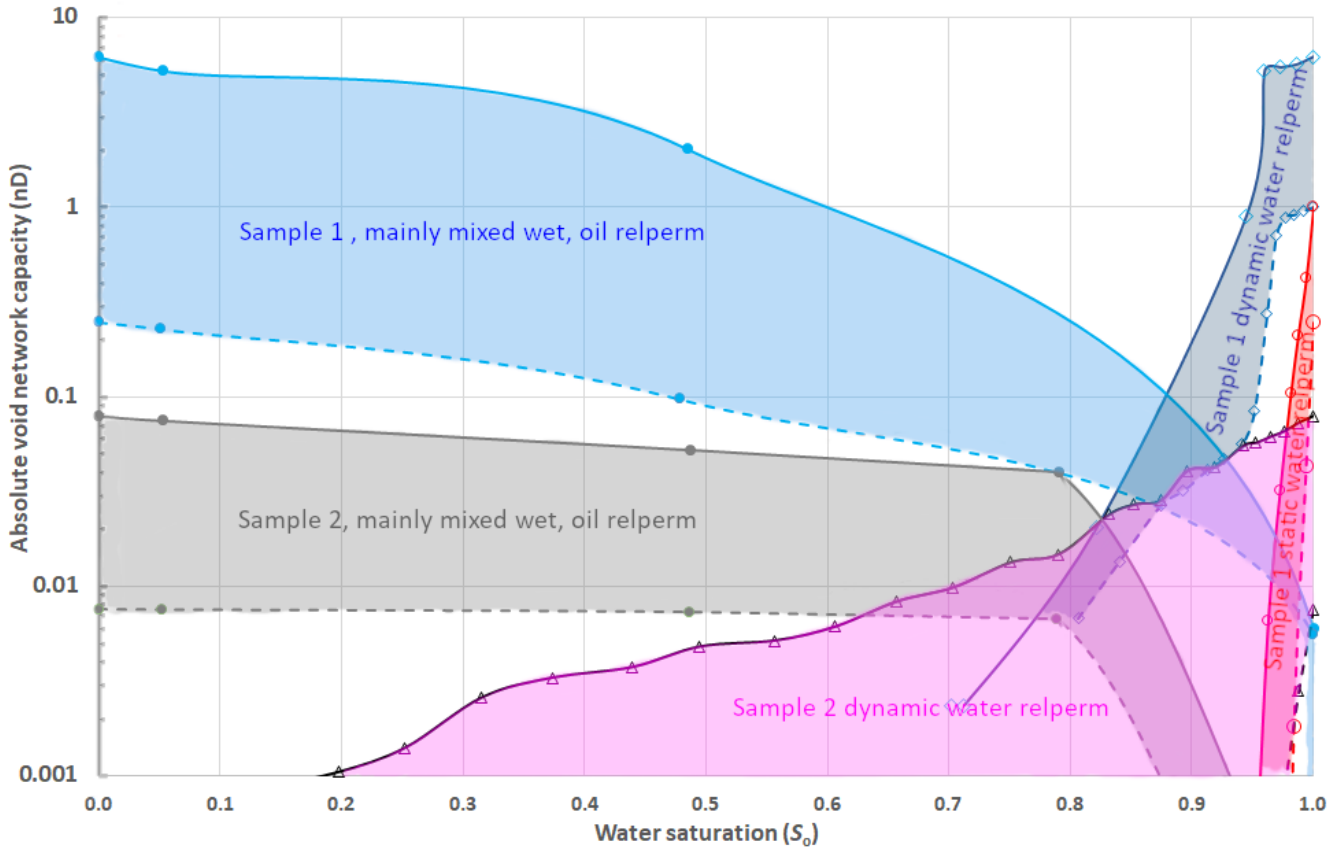

Fig. 18. Absolute relative permeabilities for Sample 1(typical) and Sample 2 (low permeability outlier) under mainly mixed wet conditions (Table 1), showing ranges of values between dynamic and static conditions on a logarithmic permeability scale.

4 Validation

As mentioned in the introduction, absolute gas permeabilities of tight-oil shale are difficult to measure, and relative oil/water permeabilities impossible. It follows that there is no method of direct validation of the relative permeability simulations reported in this work. FIB-SEM measurements cannot be used for a direct validation of the micropore and small meso-pores void sizes because, as explained previously, they cover too small a sample volume.

Indirect validation could be achieved by comparing absolute gas permeability measurements of small plugs [1] with the corresponding void network capacities. With a sufficiently large and well characterised sample set, the discrepancies could be identified as to the degree to which they are systemic within the core algorithms or specific to sample type, thus resulting in a robust calibration of the model to support its relative permeability predictions.

Meanwhile the model's fundamental algorithms have already been validated for conventional rock samples, building on the validation of the predecessor to the PoreXpert model, named Pore-Cor. Five rock samples of varying compositions of quartz, sandstone and carbonate, had permeability and porosimetry characteristics published in a British Gas database [15]. The fits of first realisations of the percolation characteristics of the inverse model to the experimental porosimetry curves are shown in Fig. 19.

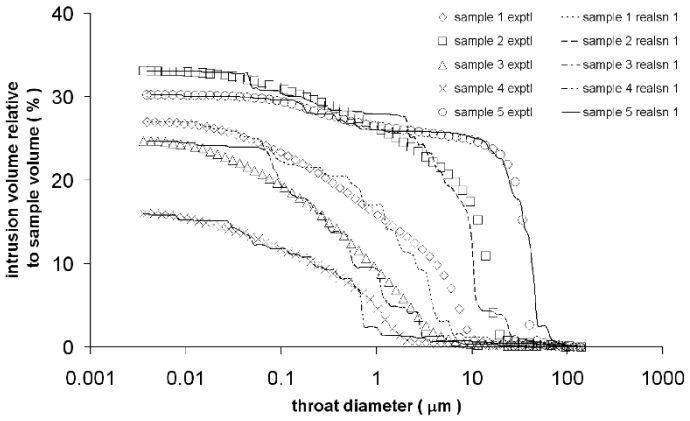

Fig. 19. Fits of the simulation to the validation samples

Fig. 20 shows experimental void sizes of one of the samples derived from image analysis of thin sections. It also shows estimates based on the traditional capillary bundle (first derivate) interpretation of the porosimetry curves, compared to several realisations of the PoreXpert's predecessor Pore-Cor and a single realisation of the PoreXpert model. Although the PoreXpert agreement is not perfect, it is nevertheless significantly better than the smaller Pore-Cor estimate, based on smaller unit cells, and orders of magnitude better than the capillary bundle approximation.

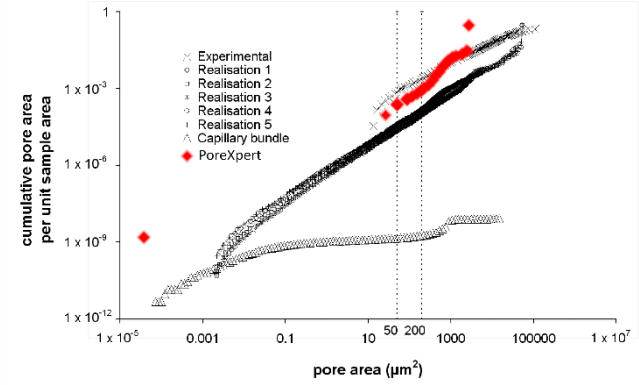

Fig. 20. Estimation of void sizes made by the inverse models Pore-Cor and PoreXpert.

We have also simulated the absolute permeability for N_2 under ambient conditions (1 atm pressure, 20° C, λ = 72 nm), Fig. 21 [16]. The network permeabilities tend to be less than the experimental values because of the simplifying flow assumptions described in Section 3.2, and the fact that the inverse modeller cannot replicate the true complexity and intricacy of void networks in most natural materials. However, the trend in permeabilities does follow the experimental trend, although in a greatly exaggerated manner. The network permeabilities do track precisely according to the mercury intrusion porosimetry curves, so a possible reason for the discrepancy is that the experimental measurements, for which we have no provenance, were measured over different sample sizes. Validation with more reliable data is therefore required.

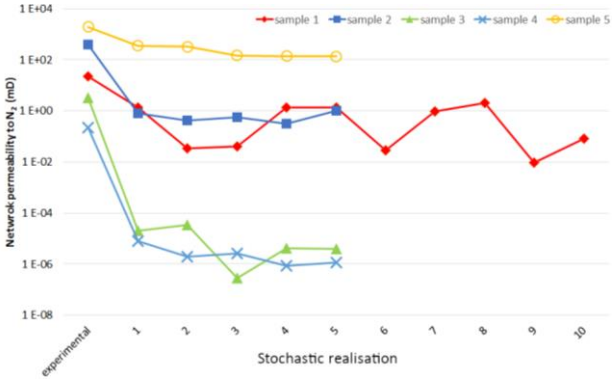

Fig. 21. Comparison of permeability estimates with experimental measurements for the five rock samples.

A current development of the inverse modeller is to base the model on porosity from image-analysed micrographs rather than pycnometry. This would require surface scans which could be assumed to be representative of the whole sample. It will provide a possible extra means of validating the model.

Ultimately, validation will need to be carried out by insertion of the relative permeability estimates into relevant oil reservoir models, and testing whether the results are realistic and a worthwhile improvement on existing Brooks-Corey type approaches. Such validation should also include assessment of the qualitative relationships listed in Table 1.

5. Conclusions

We have presented relative permeability estimates based on generic members of an actual sample set from a hydraulic fracturing play. The *a priori* estimates arise from simulated void structures generated by the inverse modelling of the experimental percolation characteristics of IPA washed samples. Once validation and calibration has been completed, the results should be capable of providing (i) quasi-static and dynamic aqueous relative permeabilities that vary according to local flow conditions, (ii) oil relative permeabilities that vary according to the oil versus aqueous wettability of the sample surfaces, and (iii) absolute as well as normalised values of permeability, for comparison between samples. The robustness of the fundamental physics behind the relative permeability simulations, and their indirect validation, gives confidence that the approach should provide a very significant and useful improvement on current reservoir characterisations of unconventional reservoirs.

The authors are grateful for the support and advice of an oil major, for useful discussions with Mike Spearing of BP, UK, and for the FIB-SEM expertise of Yang Liu of the University of Plymouth Electron Microscopy Centre. They are also grateful for the contributions of G.Maurizio Laudone of the University of Plymouth and many other programmers [16] to the development of PoreXpert.

References

1. P. Carles, P. Egermann, R. Lenormand, J.M. Lombard, SCA 2007-07 (2007).
2. M. Blunt, *Multiphase Flow in Permeable Media* (Cambridge U.P., Cambridge, 2019), p.352.
3. D.L. Luffel, F.K. Guidry, SCA 1989-8910 (1989).
4. D.L. Luffel, F.K. Guidry, JPT 1184 (1992).
5. D.A. Handwerger, D.M. Willberg, M. Pagels, B. Rowland, J. Keller. SPE 159976 (2012).
6. J. Burger, D. McCarty, R. Peacher, T. Fisher , SCA 2014-002 (2012)
7. C. Cornwall, SCA 2001-48 (2001).
8. K.L. Jones, G.M. Laudone, G.P. Matthews, Carbon, **128**:1 (2018)
9. J. Van Brakel, S. Modry, M. Svata, Powder Tech. **29**, 1 (1981)
10. G. P. Matthews, C. L. Levy, G. M. Laudone, K. L. Jones, C. J. Ridgway, I. L. Hallin, S. A. Gazze, L. Francis, W. R. Whalley, J. Schoelkopf, P. A. C. Gane. Transp. in Porous Media, **124**, 631 (2018).
11. M. Blunt, Multiphase Flow in Permeable Media (Cambridge U.P., Cambridge, 2019), section 2.2.2.
12. G.P. Matthews, C.F. Canonville , A.K. Moss, Phys. Rev. E, **73**, art: 031307 (2006).
13. J.-T. Cheng, N. Giordano, Phys. Rev. E **65**, 031206 (2002).
14. Y.K. Tovbin, R.Y. Tugazakov, A.B. Rabinovich, Theor Found Chem Eng **42**, 495–506 (2008).
15. G. P Matthews, J.W.B Matthews., https://www.porexpert.com/help2/index.html?void-size-and-permeability-val.htm, posted July 2020, accessed June 2023.
16. https://www.porexpert.com/help2/index.html?software-credits.htm, accessed July 2023.